Supplementary Materials

Comparative Study of Lithium Halide-Based Electrolytes for Application in Lithium-Sulfur Batteries

Eleonora Venezia [1,2,*,†], Pejman Salimi [1,2,†], Shanshan Liang [1,2], Silvio Fugattini [1], Lorenzo Carbone [1] and Remo Proietti Zaccaria [1,3,*]

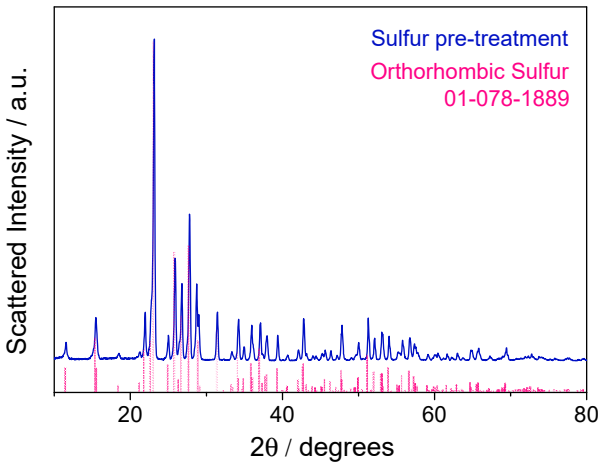

Figure S1. XRD pattern of pristine sulfur pre-treatment and the orthorhombic sulfur reference pattern.

Figure S1 shows the comparison between X-ray diffraction pattern of the pristine sulfur pre-treatment employed in the composite preparation and the orthorhombic sulfur reference pattern. All the peaks associated to the orthorhombic sulfur lattice are present in the experimental diffraction pattern. See Figure 1(a) for the sulfur-carbon composite pattern.

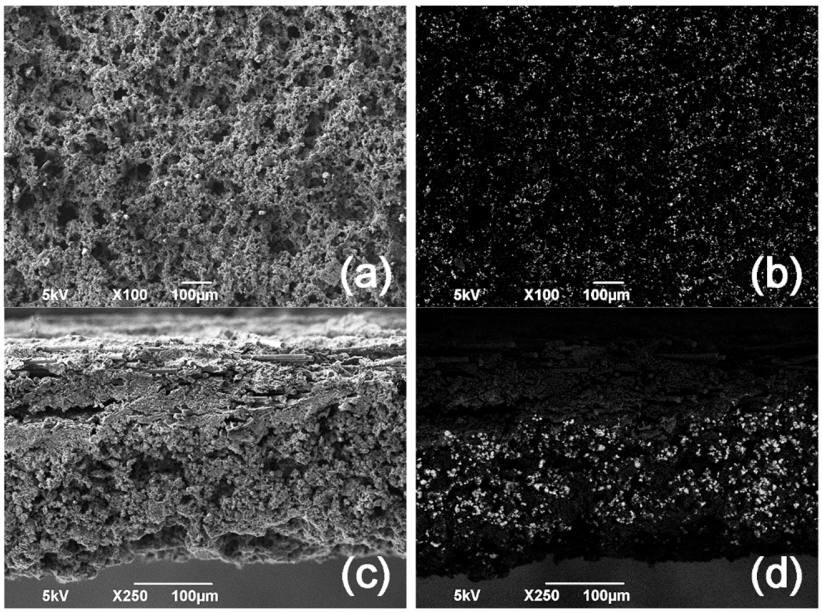

Figure S2. (a) and (b) SEM images of sulfur electrode surface and (c) and (d) of its cross section, Secondary and back scattered electrons, respectively.

Figure S2 (a) and 2S(b) depict the sulfur-carbon electrode surface (top view) showing a porous structure composed of small sulfur particles homogeneously dispersed on the electrode surface. Figure S2(c) and 2S(d) show the electrode cross section where a uniform thickness is observed, together with an homogeneous sulfur particles distribution (bright spots) along the whole thickness.

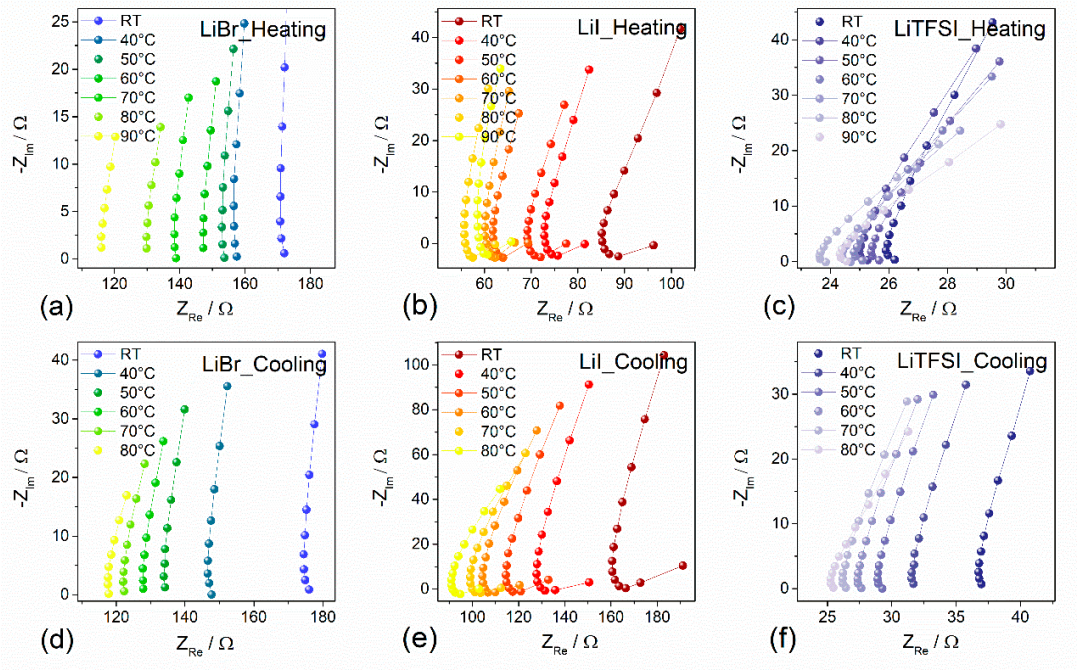

Figure S3. Electrochemical impedance spectroscopy measurements of the selected electrolyte for ionic conductivity determination.

Figure S3 reports about the conductivity measurements of each electrolytes carried out through EIS upon heating (Fig. S3 (a), (b), (c)) and cooling (Fig. S3 (d), (e), (f)) the solutions from room temperature (RT) to 90°C and back to RT. The conductivity Arrhenius plot of the electrolytes above heating is reported in Figure 3(a) of the Manuscript.

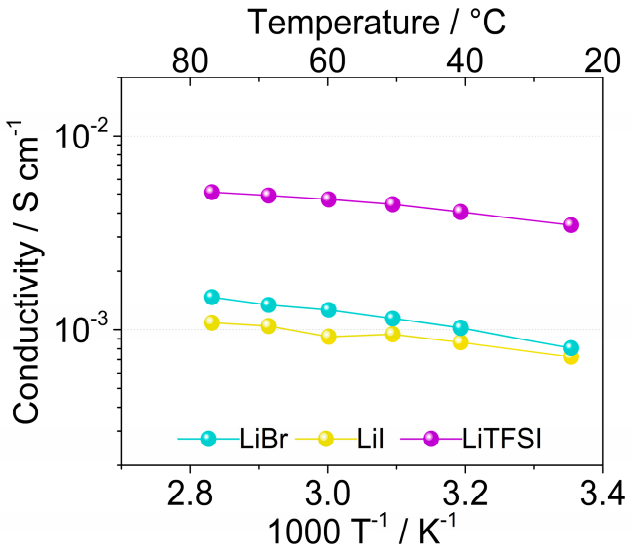

Figure S4. Comparison of electrolytes conductivity values upon cooling obtained by EIS measurements (Figure S1).

Figure S4 depicts the conductivity Arrhenius plot of the electrolytes upon cooling the solutions from 90°C to RT. The measurements obtained by increasing the temperature are reported in Figure 3a of the Manuscript. As expected, the electrolytes conductivity decreases upon temperature reduction from 90°C to room temperature.

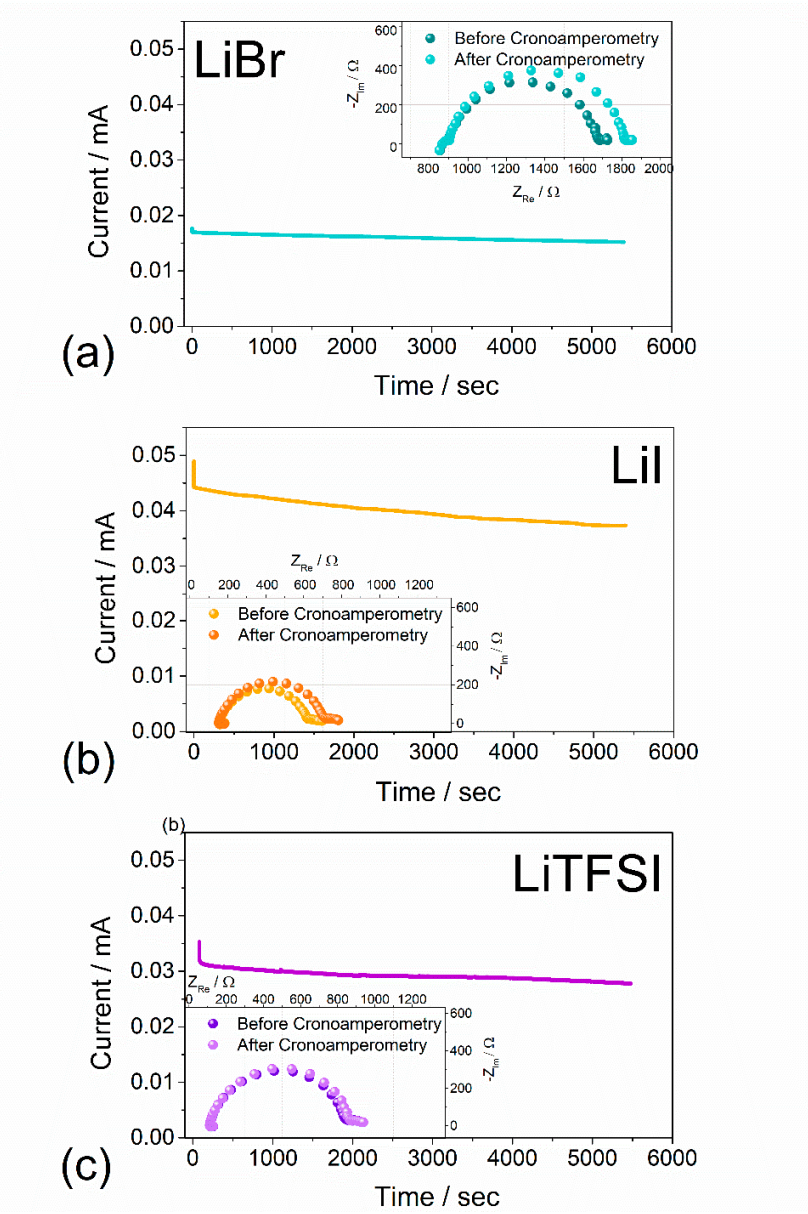

Figure S5. Chronoamperometry measurements of (a) LiBr, (b) LiI and (c) LiTFSI electrolytes and EIS tests, in inset, performed using the Bruce-Vincent technique in Swagelok-type, Li/Li symmetrical cell using DC pulse polarization of 30 mV for 90 min and electrochemical impedance spectroscopy with signal amplitude of 30 mV within 1 MHz-100 mHz frequency range.

Figure S5 shows the electrolytes chronoamperometry measurements and the EIS plots, the latter acquired before and after the chronoamperometry measurements in order to calculate the lithium transport number as in Eq.1 of the Manuscript.

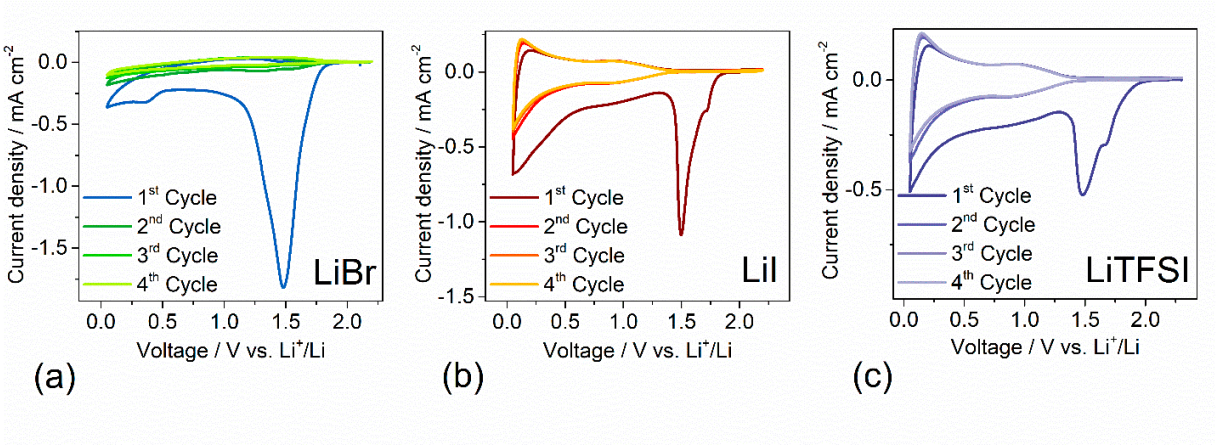

Figure S6. Cyclic Voltammetry tests of (a) LiBr, (b) LiI and (c) LiTFSI electrolytes performed in lithium-metal half-cells (2032 coin cells) using Super P on copper as working electrode, recorded at a scan rate of 0.1 mV s^{-1} in 0.01 V - 2.2 V voltage range.

Figure S6 reports the cyclic voltammetry tests of the investigated electrolyte. As reported in Figure 4(a) of the Manuscript, the first cathodic peaks could be ascribed to the SEI formation, while the peak at lower voltage (about 0.01V) is related to the Li-ion intercalation. The peak associated with the SEI film deposition disappear after the first cycle. Only the intercalation and de-intercalation peaks are visible in the following cycles.

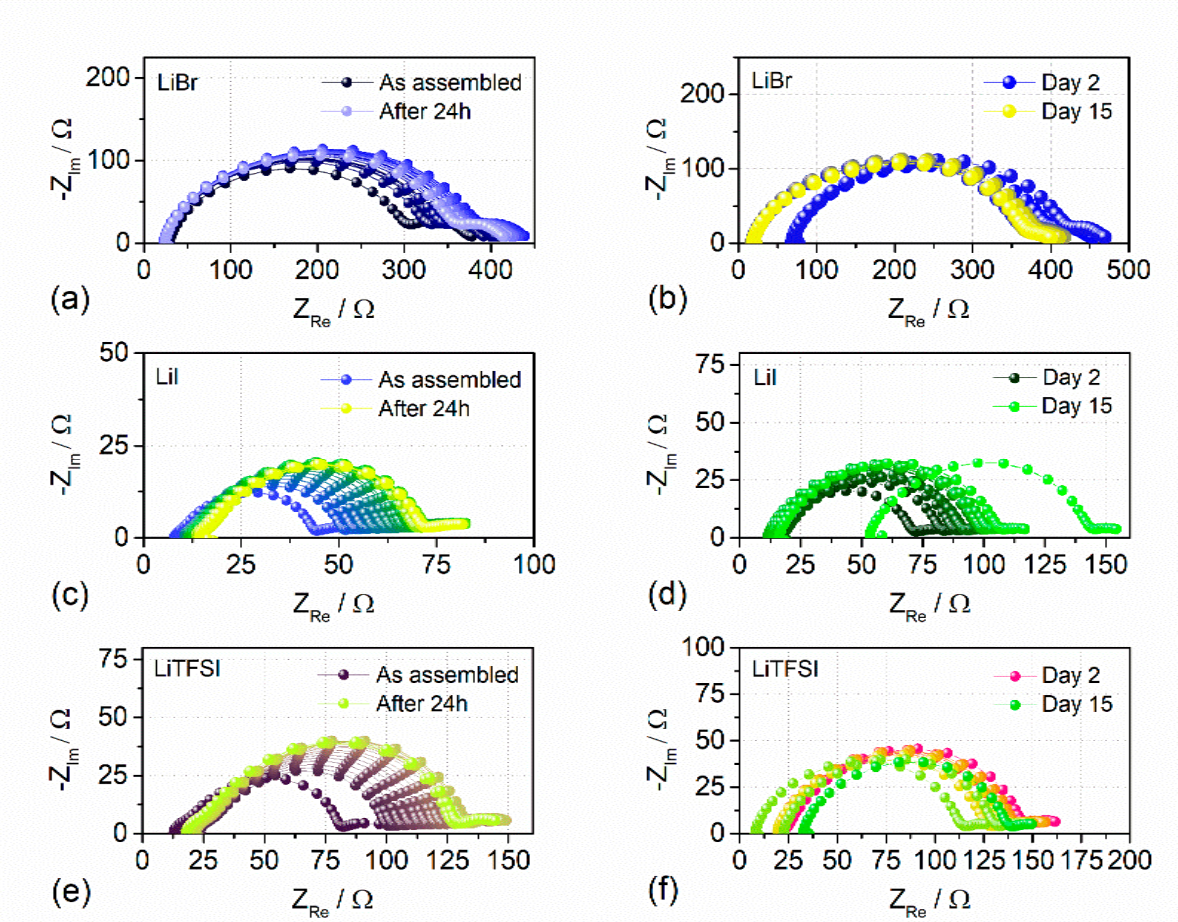

Figure S7. Nyquist plots relative to the electrochemical impedance spectroscopy performed applying a signal amplitude of 10 mV within 1 MHz-100 mHz frequency range to investigate the Li-electrolyte interface resistance evolution over time.

Figure S7 reports the Nyquist plots related to the electrochemical impedance spectroscopy measurements performed in symmetrical Li cells containing the four electrolytes over a period of 15 days. The evolution over time of the lithium interfacial resistance is shown in Figure 4(c) and is obtained through the NLLSQ fit of the impedance spectra. After the cells assembly, the EIS measurements were carried out every hour during the first day and once per day for the remaining testing period, as reported in Figure S7(a) and (b) for LiBr, Figure S7(c) and (d) for LiI and Figure S7(e) and (f) for LiTFSI, respectively.

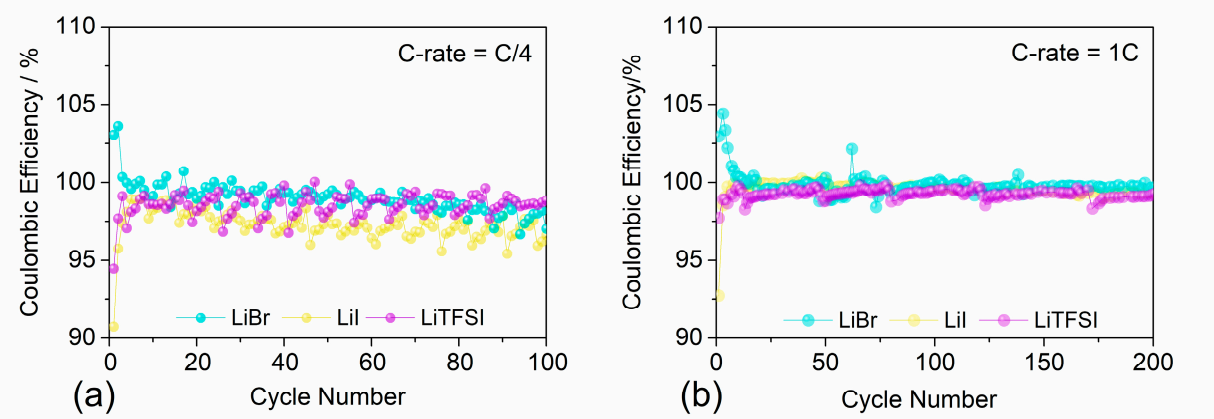

Figure S8. Coulombic efficiency of the galvanostatic cycling performed at C/4 and 1C.

Figures S8(a) and (b) report about the coulombic efficiency regarding the galvanostatic cycling measurements of the lithium-sulfur cells tested at C/4 and 1C, respectively (Figure 5 of the Manuscript).

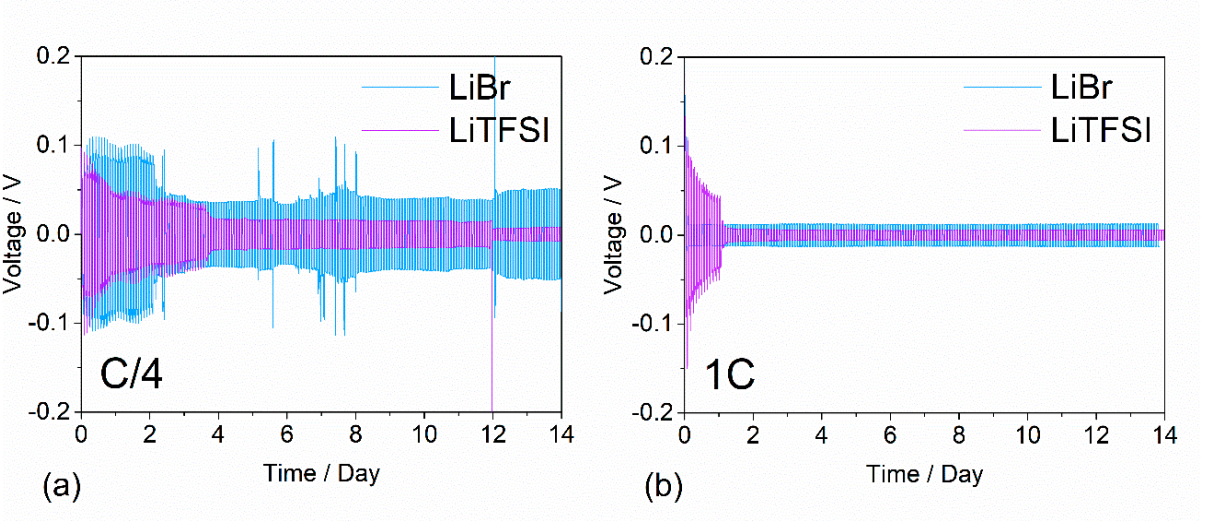

Figure S9. Stripping/deposition test carried out in symmetrical Li/Li cells at (a) C/4 and (b) 1C on LiTFSI and LiBr electrolyte samples.

Figure S9 shows the lithium stripping/deposition tests carried out on LiTFSI and LiBr samples at the current rate of C/4 and 1C, in order to reproduce the behavior during cycling.

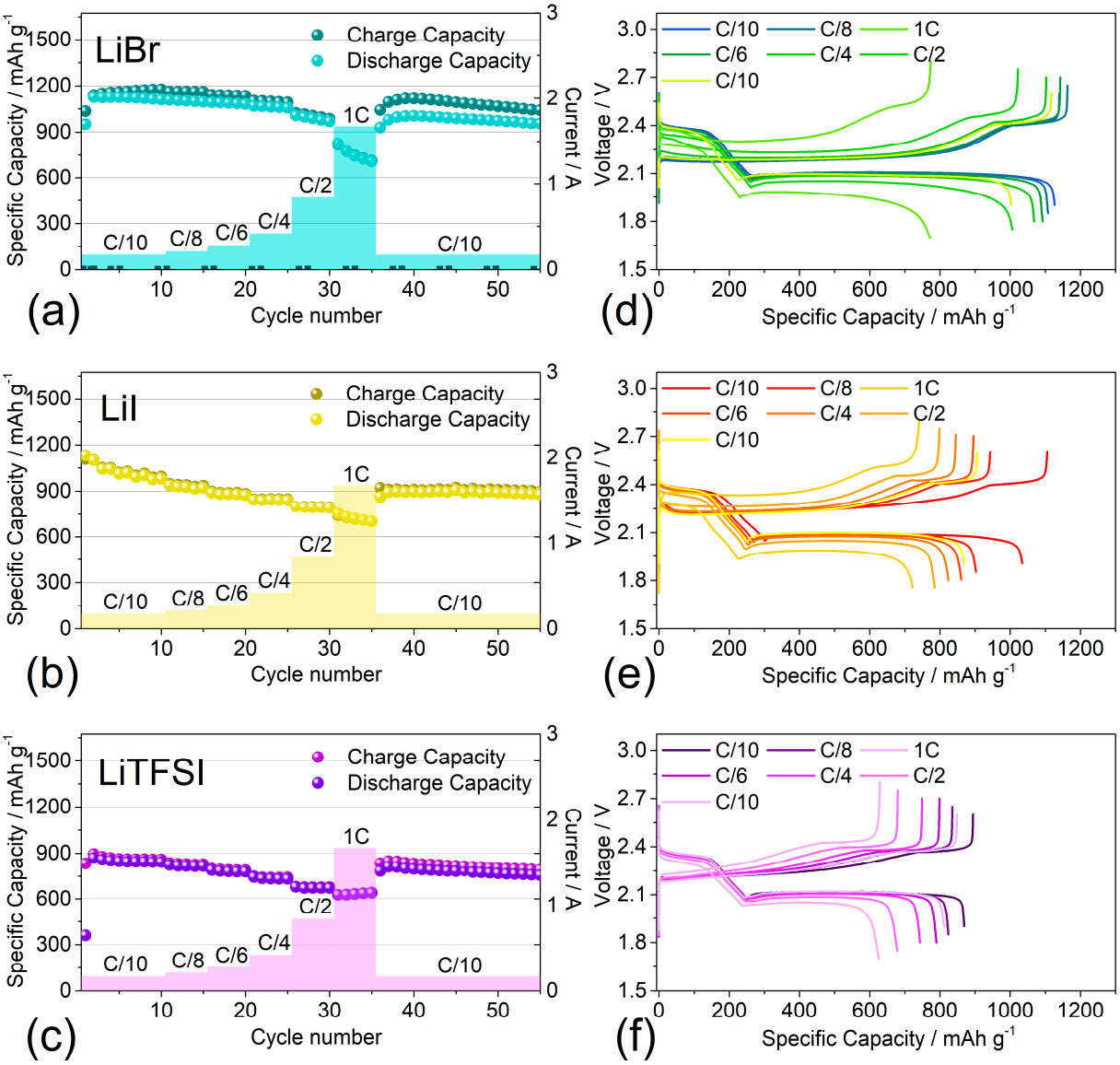

Figure S10. Rate capability test: (a), (d) LiBr, (b), (e) LiI and (c), (f) LiTFSI carried out in Li-S cells in a 1.7 V – 2.8 V voltage range at C/10, C/8, C/6, C/4, C/2, 1C current rates (1C=1675 mA g^{-1}).

The rate capability tests of LiBr, LiI and LiTFSI-based cells are reported in Figure S10. The cells containing the lithium halides salts-based electrolytes showed a specific capacity increase with respect to the reference electrolyte employing LiTFSI, as also confirmed by the galvanostatic cycling tests at 1C and C/4 reported in Figure 5 of the Manuscript. The cells employing LiBr-based electrolyte release the highest capacity at C/10 of about 1180 mAh g^{-1} and show a low charge/discharge polarization.